Editors' Suggestion

Millijoule Terahertz Radiation from Laser Wakefields in Nonuniform Plasmas

Linzheng Wang,[1,2,*] Zhelin Zhang,[1,2,3,*] Siyu Chen,[1,2] Yanping Chen,[1,2,†] Xichen Hu,[1,2] Mingyang Zhu,[1,2] Wenchao Yan,[1,2] Hao Xu,[1,2] Lili Sun,[1,2] Min Chen,[1,2] Feng Liu,[1,2] Liming Chen,[1,2] Jie Zhang,[1,2,3] and Zhengming Sheng[1,2,3,‡]

[1]*Key Laboratory for Laser and Plasma (Ministry of Education), School of Physics and Astronomy, Shanghai Jiao Tong University, Shanghai 200240, China*

[2]*Collaborative Innovation Centre of IFSA, Shanghai Jiao Tong University, Shanghai 200240, China*

[3]*Tsung-Dao Lee Institute, Shanghai Jiao Tong University, Shanghai 201210, China*

(Received 9 December 2023; accepted 12 March 2024; published 16 April 2024)

We report the experimental measurement of millijoule terahertz (THz) radiation emitted in the backward direction from laser wakefields driven by a femtosecond laser pulse of few joules interacting with a gas target. By utilizing frequency-resolved energy measurement, it is found that the THz spectrum exhibits two peaks located at about 4.5 and 9.0 THz, respectively. In particular, the high frequency component emerges when the drive laser energy exceeds 1.26 J, at which electron acceleration in the forward direction is detected simultaneously. Theoretical analysis and particle-in-cell simulations indicate that the THz radiation is generated via mode conversion from the laser wakefields excited in plasma with an up-ramp profile, where radiations both at the local electron plasma frequency and its harmonics are produced. Such intense THz sources may find many applications in ultrafast science, e.g., manipulating the transient states of matter.

DOI: 10.1103/PhysRevLett.132.165002

Terahertz (THz) pulses with energy at the millijoule level can provide electric fields exceeding 10 MV/cm, which can facilitate applications in many fields [1]. For instance, high-field THz radiation can be used to manipulate [2,3] and diagnose [4] electron bunches. It was reported that THz fields over the MV/cm level can engineer the transient states of matter [5], i.e., lattice vibrations [6], molecular rotations [7,8], and spin waves [9,10]. Moreover, intense THz radiation can provide a new technique to study nonlinear effects in materials [11–13], e.g., hot Dirac fermions excitation induced THz high harmonics in graphene [13].

Nowadays, there have been a few approaches to generate millijoule-level THz sources. The mainstream methods are based either on coherent transition radiation (CTR) of electron bunches [14–17] or by optical rectification (OR) in crystals [18–21]. THz radiation from CTR requires high-energy electron bunches, which can be generated either by conventional accelerators [14,15] or by laser wakefield accelerators [16,17]. Recently, experimental measurements of multimillijoule broadband THz radiation in the forward direction via CTR due to laser wakefield-accelerated high charge electrons were reported [16]. Also narrow-band THz radiation in the forward direction due to laser wakefields excited in nonuniform plasma was investigated theoretically and numerically [22]. Alternatively, it was reported that millijoule-level THz radiation can be generated through OR by irradiating a diameter-expanded large laser beam on either lithium niobates [19,20] or DSTMS [21]. However, such methods are limited by the cost and difficulties in preparing large-size crystals as well as the collecting optical elements. On the other hand, it has been proposed theoretically that high field THz emission can be generated directly from a laser wakefield excited in nonuniform plasmas via linear mode conversion [23–25]. The emission is usually found in the backward direction with broad spectrum determined by the plasma density profile. Pioneering experimental studies on THz emission from short pulse laser interactions with gas and solid targets were made many years ago [26,27], where the output energy is at the microjoule level.

In this Letter, we report the experimental measurement of millijoule-level THz radiation in the backward direction through the excitation of laser wakefields when an intense femtosecond laser pulse is focused onto a gas nozzle. By utilizing frequency-resolved energy measurements, it is found that the THz spectrum is broadband with two peaks located around 4.5 and 9.0 THz, respectively. The high frequency peak emerges when the laser energy is relatively high above 1.2 J in our experiment, at which electron acceleration in the laser wakefields is also detected. Theoretical analysis and simulations identify that the dominant mechanism of the intense THz radiation is the mode conversion from the laser wakefields excited in the nonuniform density profile formed by the gas nozzle.

The experiment was performed on a 200 TW Ti:sapphire laser facility under the single-shot mode in Shanghai Jiao Tong University, with the setup schematically shown in

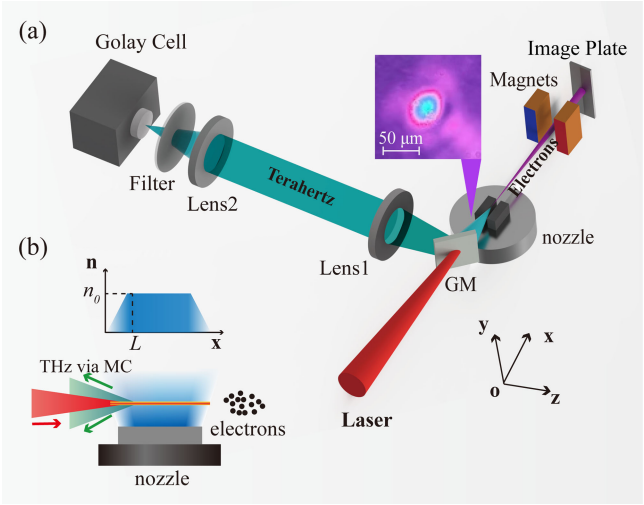

FIG. 1. (a) Schematics of the experimental setup. The inset shows the image of the laser focal spot. (b) Schematic of the laser wakefield excitation and THz radiation in the nozzle, where the red arrow and green arrows show the laser injection direction and THz radiation direction, respectively. The inset shows the approximated gas density profile with an up-ramp length L.

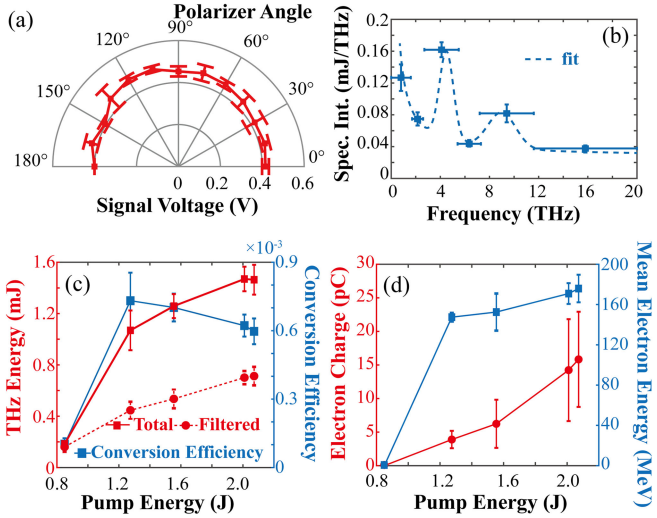

FIG. 2. Experimental results. (a) The measured THz signal voltage at different polarizer angles. (b) THz spectra measured by inserting lowpass filters in front of the Golay cell under the laser energy of 2.07 J, where the dashed line is a fitting of the radiation spectrum. (c) Total THz energy, lowpass filtered THz energy with cutoff frequency of 5.5 THz, and the calculated energy conversion efficiency for different pump energy. (d) The measured electron charge and the mean energy of accelerated electrons from laser wakefields under different laser energy. Note that each data point is obtained by averaging ten laser shots.

Fig. 1(a). With only its first stage of amplification works, an 800 nm wavelength laser with pulse duration of 35 fs (FWHM) and energy tunable within 2.2 J is focused on a nozzle in a vacuum chamber by an off-axis parabolic mirror with 2 m focal length. A wave-free supersonic pulsed gas jet system (Smartshell Co. Ltd.) with nozzle of 1×4 mm in the transverse cross section is used in our experiment, which is synchronized with the laser by the trigger of a digital delay generator DG535. A mixture gas of 98% helium and 2% nitrogen is used here with the back pressure fixed at 0.45 Mpa. Such a nozzle produces a trapezoid molecular density profile with peak density n_0 of $\sim 2 \times 10^{18}$ cm^{-3} as shown in inset of Fig. 1(b). The typical length of the density ramp at the edge of the nozzle gas flow is $L = 0.8$ mm [28]. According to theory [23–25], THz radiation emitted via mode conversion is found in the backward direction as shown in Fig. 1(b). In our experiment, the backward THz radiation is reflected by a center-drilled golden mirror from the laser axis, and collected by a pair of polymethyl pentene (TPX) lens (lens 1 and lens 2) with 10 cm focal length, as shown in Fig. 1(a). The energy of the THz radiation is measured by a Golay cell, in front of which a 200 μm silicon wafer is embedded for blocking other band emission.

We have carried out a series of measurements on the THz radiation to investigate its characteristics by keeping the Golay cell at the THz beam center. The calibration method of the THz radiation energy can be found in the Appendix of the Letter. First, we insert a THz polarizer before the Golay cell to check the polarization of the THz radiation. As shown in Fig. 2(a), the THz energy is basically the same under different polarizer angles within 180 degrees.

We have conducted frequency-resolved THz energy measurement by inserting a set of THz lowpass filters, which is described in detail in the Appendix. The distribution of the spectral intensity $E_j/\delta\omega_j$ under the pump energy of 2.07 J is calculated as shown in Fig. 2(b), where E_i is the measured energy with the i th filter and $\delta\omega_j$ is the bandwidth of the j th selected frequency band. It is clearly shown that the spectrum exhibits three peaks. The first peak lies around zero frequency, which could be attributed to the Sommerfeld mode [29]. The second peak lies around 4.5 THz. The third one lies around 9 THz, which is basically the second harmonic of the second peak.

Then, we change the pump energy from 0.85 to 2.07 J to investigate the appearance of the two high-frequency peaks. In Fig. 2(c), it is shown that the low frequency component below 5.5 THz increases almost linearly with the laser energy, while the high frequency component above 5.5 THz is observed experimentally at the laser energy of 1.26 J. The total THz energy reaches about 1.47 mJ with the pump energy of 2.07 J. The peak conversion efficiency reaches $\sim 10^{-3}$ at the pump energy of 1.26 J as shown by the blue line in Fig. 2(c). Then it gradually decreases with the pump energy. In addition to the measurement of THz emission, electron acceleration from the laser wakefields is also detected. The calibrated mean energy of accelerated electrons under different pump energy and the total electron charge are shown in Fig. 2(d). The total electron charge is obtained by integrating over the electron spectrum. In our

experiment, the energy spectra of the electron bunch in the forward direction are detected by the deflection of the magnetic field. The accelerated electron bunch appears at the pump energy of 1.26 J, which is accompanied with the appearance of high frequency components on the THz radiation as shown in Fig. 2(c).

As shown in the inset of Fig. 1(a), we measured the laser beam diameter at the front edge of the nozzle, which is about 26 μm (FWHM). Thus, the corresponding normalized amplitude of the laser pulse a_0 is about from 0.86 to 1.34 for the pump energy from 0.85 to 2.07 J. Here, a_0 is related with the laser peak intensity through $I\lambda_0^2 = a_0^2 \cdot 1.37 \times 10^{18}\ \mathrm{W\,cm^{-2}\,\mu m^2}$ with $\lambda_0 = 0.8\ \mu\mathrm{m}$ the laser wavelength. When the laser pulse is focused into the nozzle, it ionizes the gas and forms the plasma wake. In the range of $a_0 > 1$, the plasma wake becomes highly nonlinear and harmonics at the electron plasma frequency $\omega_N = N\omega_p$ appears [30–32], where $\omega_p = \sqrt{4\pi n_e(x)e^2/m}$ is the plasma frequency with x the propagation axis and N the harmonic order.

The gas mixture used in our experiment can result in electron acceleration via ionization injection [33–35], where the helium electrons and L-shell nitrogen electrons can be ionized in the leading edge of the laser pulse, forming the plasma wake due to the ponderomotive force. The K-shell nitrogen electrons ionized around the laser peak can be trapped and continuously accelerated in the plateau area as shown in Fig. 1(b). In our experimental conditions, from the THz spectrum, we deduce that the nonlinear plasma wake occurs at the pump energy of 1.26 J when the accelerated electrons occur in Fig. 2(d) with the normalized amplitude $a_0 = 1.05$, which is possible for ionization injection as the self-focusing in the low-density ramp enhances the laser amplitude [35].

In the following, we analyze the mechanism responsible for the THz emission observed in our experiment. As the laser pulse has a Gaussian profile transversely, the excited plasma wake is expected to have a transverse wave vector k_y. Assume the nonlinear wakefield takes a transverse Gaussian profile $f(y) = \exp(-2y^2/w^2)$ with w the beam waist, then the transverse wave vector $k_{y,N}$ for the harmonic order N has the same transverse distribution of $F(k_{y,N}) = \sqrt{\pi w^2/2}\exp(-k_{y,N}^2 w^2/8)$ by making two-dimensional Fourier transformation. As a result, the wave vector of the plasma wake has an angle $\tan\theta_N = k_{x,N}/k_{y,N}$, where $k_{x,N}$ is the longitudinal wave vector. In this case, the wakefield can be converted to electromagnetic radiation through mode conversion when $k_{x,N}$ evolves to zero. The latter is found when the laser wakefield is excited in plasma with a density up-ramp [23–25]. Now that the wakefield is nonlinear, one needs to check emission for the harmonics of plasma wake.

For simplicity, assume that the wake phase velocity $v_{ph} = c$ for tenuous plasma [22], the local plasma wake phase for each harmonic ω_N can be written as $\psi_N = -N\omega_p(x)(t - x/c)$. Considering a plasma density of $n_e = n_{e0}x/L$,the wave vector of the local plasma wake reads

$$k_{x,N} = \frac{\partial \psi_N}{\partial x} = N\omega_p(x)(3x - ct)/2x. \tag{1}$$

Then following the spatiotemporal line $x = ct/3$, the wave vector of each harmonic of the plasma wake $k_{x,N} = 0$. This suggests that the harmonics of the nonlinear plasma wake can be converted into THz radiation through the mode conversion process on the same space-time line.

We have conducted two-dimensional (2D) particle-in-cell (PIC) simulations using the code OSIRIS [36] to investigate the characteristics of the THz radiation in the nonlinear plasma wake regime. To save the computing resources, only a plasma up-ramp with length $L = 0.8$ mm is considered. As the laser is intense enough to ionize all the helium electrons, the maximum plasma density is taken as $n_{e0} = 2n_0$. The laser parameters are basically the same as the experimental ones. The laser is incident with a pulse duration of $12T_0$, spot radius of $20\lambda_0$, as well as s polarization. The latter enables one to distinguish it from the p-polarized THz radiation emitted from the laser wakefields in 2D simulations.

Snapshots of the magnetic field B_z at $t = 400T_0$ with $a_0 = 1.2$ are shown in Fig. 3(a). It can be clearly seen that strong THz radiation is radiated in the backward direction toward vacuum. As the normalized laser intensity $a_0 > 1$, the laser wakefield is highly nonlinear and appears in the form of bubbles at the tail of the laser pulse shown in Figs. 3(b) and 3(c) for the electron density and electric field, respectively. At $t = 3x/c$, the plasma wake will experience a reversal in the direction of the wave vector accompanied by the vanish of plasma wake amplitude as detected in previously research [37]. In Fig. 3(c), such a phenomenon appears in the white box area. At the same time, the backward radiation associated to the linear mode conversion appears in Fig. 3(a) as the white arrow shows. The spatiotemporal plot of the on-axis longitudinal electric field E_x is shown in Fig. 3(d). The vanish of the plasma wake strictly follows the line of $x = ct/3$ (the black solid line). Meanwhile, the wave vector of plasma wake changes its sign along the mode conversion line.

The waveform of the collected THz radiation at $25\lambda_0$ away from the left boundary is shown in Fig. 3(e). The relation of collecting time t_0 with the corresponding plasma longitudinal position x_0 can be derived as $t_0 = 25T_0 + 3x_0/c + 2x_0/c$. Here, the first term is related to the collecting position, the second and third terms are brought by the appearance of mode conversion and propagating distance inside the plasma. The THz radiation has positive chirp as the plasma wake in higher plasma density region is excited later. Besides, the radiation is

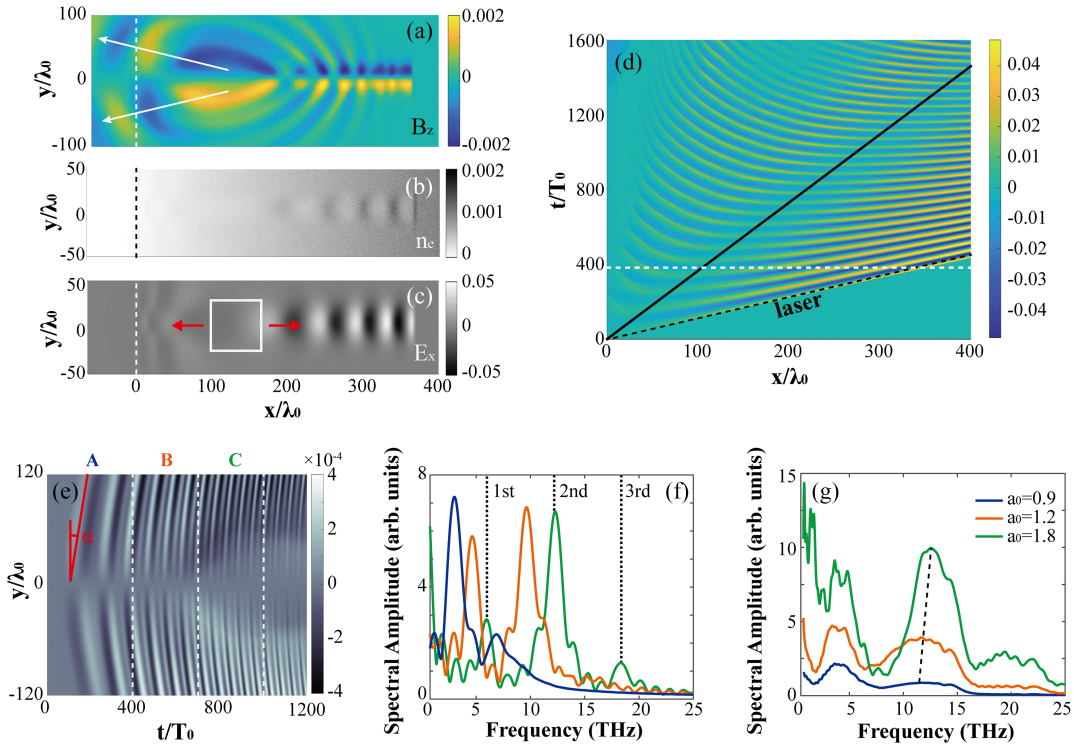

FIG. 3. 2D PIC simulation results. Snapshots of magnetic field B_z (a), electron density n_e (b), and electric field E_x (c) at $t = 400T_0$ with the peak laser amplitude $a_0 = 1.2$. Dashed lines show the plasma-vacuum boundaries. (d) Spatiotemporal plot of the on-axis longitudinal electric field E_x. (e) THz radiation waveform E_y collected at $25\lambda_0$ away from the left boundary, where the white dashed lines divide the time into intervals of A $[0, 400T_0]$, B $[400T_0, 700T_0]$, C $[700T_0, 1000T_0]$. (f) The amplitude spectra of the THz radiation, where the blue, orange, and green lines correspond to the radiation from the time intervals A, B, and C shown in (e), respectively. The black dashed lines mark the positions of the fundamental, second, and third harmonics for radiation within the time interval C. (g) The collected spectra of the THz radiation under different pump energy. The electric and magnetic fields in this figure are normalized by $m\omega_0 c/e$, while the electron density is normalized by n_c, in which $n_c = 1.756 \times 10^{21}$ cm^{-3} is the critical plasma density of 800 nm wavelength.

radially polarized, which consistent with the experimental results in Fig. 2(a). The radiation conical angle is $\alpha \propto 1/k_p w$ as marked in Fig. 3(e), which also depends upon the radiation frequency [25]. The conical angle drops from about 36° in region A to about 19° in region C with higher radiation frequency under the given conditions. Moreover, the near field amplitude reaches up to about 1.6 GV/m and the energy conversion efficiency from laser exceeds 2×10^{-3}. The collecting angle in our experiment is limited to the aperture of the TPX lens, leading to the loss on conversion efficiency in Fig. 2(c) compared to the simulation result. The spectra at different time intervals in Fig. 3(e) are shown in Fig. 3(f). The separated spectra exhibit multiple peaks. For example, the spectrum of time interval C exhibits three peaks at the fundamental, second, and third harmonic of the plasma frequency around 6 THz emitted from the plasma region $x_0 = [135\lambda_0, 195\lambda_0]$. They radiate at the same time, in agreement with our analysis given above. Because of the positive chirp, the peaks of the harmonics are blueshifted with a larger time delay.

Figure 3(g) shows the total THz spectra obtained with different laser amplitudes from $a_0 = 0.9$ to 1.8. At $a_0 = 0.9$, the THz radiation is dominated by the fundamental wave. The wake amplitude of the fundamental wave scales linearly with a_0^2 [35], which is analogous to our simulation results in Fig. 3(g). Compared to the experimental result in Fig. 2(c), however, it suggests that the THz energy almost linearly increases with the pump energy. As the pump energy is enhanced, the beam waist w decreases due to severer self-focusing, consequently the THz conical angle increases according to $\alpha \propto 1/k_p w$. Thus, the above discrepancy could be due to more serious loss on the fundamental wave excited with enhanced pump energy in experimental measurement. The amplitudes of the high harmonic components also increase with the pump energy, in particular, when the plasma wakefield becomes highly nonlinear. Therefore, the second harmonic component is found to increase with the pump energy more quickly than the fundamental wave, as shown in Fig. 3(g). Since the higher frequency components associated with higher plasma density boosts with higher pump energy more quickly, the peak at the high frequency is blueshifted with a higher pump laser amplitude.

In conclusion, we report experimental measurements of millijoule-level backward THz radiation from laser

wakefields excited in nonuniform plasmas. Under our gas target conditions, the THz radiation spectra exhibit two peaks at about 4.5 and 9.0 THz, respectively. The energy of the lower frequency radiation increases nearly linearly as the drive laser energy boosts, while the energy of the higher frequency radiation emerges at the laser energy of 1.26 J. In this case, accelerated electrons from the wakefields are also measured in forward direction. Theoretical analysis and 2D PIC simulations show that the radiation is due to laser wakefield excitation and subsequent mode conversion in the plasma density up-ramp. Through the same mechanism, the plasma wake can radiate harmonics of the plasma frequency when the laser pulse is at relativistic high intensity. The conversion efficiency measured is as high as $\sim 10^{-3}$ with tunable spectrum determined by the plasma density. Such high-field THz radiation may find applications in many areas and it may provide a useful diagnosis of the laser wakefields.

The authors would like to acknowledge the OSIRIS Consortium, consisting of UCLA and Instituto Superior Técnico for providing access to the OSIRIS4.0 framework. This work is supported by National Natural Science Foundation of China (Grants No. 12074250, No. 11991073, No. 11991074, and No. 12135009) and Science and Technology Commission of Shanghai Municipality (Grant No. 22JC1401900).

Appendix: Experimental Methods.—THz energy calibration: To calibrate the THz energy, we have considered the response coefficient of the Golay cell, the absorption of the transmissive elements, and the size of the focal spot. First, the calculated response coefficient is $\eta = 15.16\ \mu\mathrm{J/V}$ by the calibration using an 800 nm laser pulse with μJ-level energy. Second, the TPX lens, silicon wafer, and the TPX chamber window in the detection path introduce a total transmittance of about $T = 0.185$ in the THz region. In addition, as the THz spot is much larger than the aperture of the Golay cell, we have conducted a spatial scanning in both horizontal and vertical directions [38]. The scanned THz beam profile exhibits a standard Gaussian beam with the beam radius of $r = 11.10$ mm, as shown in Fig. 4. Finally, the calibration efficiency between the Golay cell signal at the THz beam center and the total THz energy can be derived as

$$\alpha_{\mathrm{THz}} = \frac{\eta r^2}{TS}\pi = 1.16\ \mathrm{mJ/V}, \tag{A1}$$

where S is the surface area of the Golay cell.

Frequency-resolved THz energy measurement: Considering that the spectral curves of different filters have distinct line shapes, we have taken the linear superposition method for different frequency bands. And the frequency bands are divided by the cutoff frequencies of the filters introduced in the experiment. The transmittance of

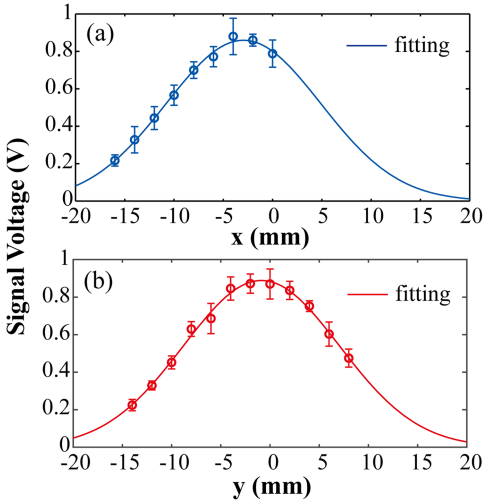

FIG. 4. Spatial scanning results on the THz radiation along the horizontal (a) and vertical (b) directions, respectively. The solid lines give the Gaussian fitting results with the waist of about 11.10 mm.

the i th filter within the j th frequency band can be represented as T_{ij}, which is taken as the transmittance on the central frequency within the j th band. By inserting the whole set of filters, the relation between the measured energy and the real THz energy with different filters can be expressed as

$$[T_{ij}][E_j] = [E_i]. \tag{A2}$$

Here, E_i is the measured energy with the ith filter, and E_j is the real THz energy within the j th frequency band.

In our experiment, a set of terahertz lowpass filters (LPF3.2, LPF5.5, LPF10.9, LPF14.3, LPF23.1 from TYDEX) is used for frequency-resolved measurements. The frequency bands are divided by the cutoff frequencies of the filters, where the transmittance is decayed to the $1/e^2$ level of the transmittance maximum. The cutoff frequencies corresponding to these filters are given as [1.6 THz, 2.6 THz, 5.5 THz, 7.3 THz, 11.6 THz, 20 THz], in which 20 THz is introduced by the cutoff frequency of the TPX lens [39]. Then, the transmittance of the i th filter in the central frequency of jth band can be denoted as

$$[T_{ij}] = \begin{bmatrix} 0.45 & 0 & 0 & 0 & 0 & 0 \\ 0.50 & 0.20 & 0 & 0 & 0 & 0 \\ 0.65 & 0.65 & 0.35 & 0 & 0 & 0 \\ 0.85 & 0.75 & 0.12 & 0.15 & 0 & 0 \\ 0.70 & 0.50 & 0.25 & 0.18 & 0.08 & 0 \\ 1.00 & 1.00 & 1.00 & 1.00 & 1.00 & 0.50 \end{bmatrix}. \tag{A3}$$

Note that the last row in T_{ij} corresponding to 20 THz is normalized since the transmittance of the TPX lens has

already been counted in the energy calibration part. The last numerical value 0.50 is the normalized transmittance of TPX lens at the frequency of 15.8 THz, which is the central frequency of the last band.

*These authors contributed equally to this work.
†Corresponding author: yanping.chen@sjtu.edu.cn
‡Corresponding author: zmsheng@sjtu.edu.cn

[1] X. C. Zhang, A. Shkurinov, and Y. Zhang, Nat. Photonics **11**, 16 (2017).
[2] L. Zhao, H. Tang, C. Lu, T. Jiang, P. Zhu, L. Hu, W. Song, H. Wang, J. Qiu, C. Jing *et al.*, Phys. Rev. Lett. **124**, 054802 (2020).
[3] D. Zhang, A. Fallahi, M. Hemmer, X. Wu, M. Fakhari, Y. Hua, H. Cankaya, A. Calendron, L. E. Zapata, N. H. Matlis *et al.*, Nat. Photonics **12**, 336 (2018).
[4] R. K. Li, M. C. Hoffmann, E. A. Nanni, S. H. Glenzer, M. E. Kozina, A. M. Lindenberg, B. K. Ofori-Okai, A. H. Reid, X. Shen, S. P. Weathersby, J. Yang, M. Zajac, and X. J. Wang, Phys. Rev. Accel. Beams **22**, 012803 (2019).
[5] T. Kampfrath, K. Tanaka, and K. A. Nelson, Nat. Photonics **7**, 680 (2013).
[6] I. Katayama, H. Aoki, J. Takeda, H. Shimosato, M. Ashida, R. Kinjo, I. Kawayama, M. Tonouchi, M. Nagai, and K. Tanaka, Phys. Rev. Lett. **108**, 097401 (2012).
[7] F. Blanchard, J. E. Nkeck, L. Guiramand, S. Zibod, K. Dolgaleva, T. Arikawa, and K. Tanaka, Optica **9**, 980 (2022).
[8] A. Beer, R. Damari, Y. Chen, and Sharly Fleischer, J. Phys. Chem. A **126**, 3732 (2022).
[9] T. Kurihara, M. Bamba, H. Watanabe, M. Nakajima, and T. Suemoto, Commun. Phys. **6**, 51 (2023).
[10] R. Salikhov, I. Ilyakov, L. Körber, A. Kákay, R. A. Gallardo, A. Ponomaryov, J. Deinert, T. V. A. G. de Oliveira, K. Lenz, J. Fassbender *et al.*, Nat. Phys. **19**, 529 (2023).
[11] H. A. Hafez, S. Kovalev, K. Tielrooij, M. Bonn, M. Gensch, and D. Turchinovich, Adv. Opt. Mater. **8**, 1900771 (2020).
[12] S. Kovalev, H. A. Hafez, K. Tielrooij, J. Deinert, I. Ilyakov, N. Awari, D. Alcaraz, K. Soundarapandian, D. Saleta, S. Germanskiy *et al.*, Sci. Adv. **7**, eabf9809 (2021).
[13] H. A. Hafez, S. Kovalev, J. Deinert, Z. Mics, B. Green, N. Awari, M. Chen, S. Germanskiy, U. Lehnert, J. Teichert *et al.*, Nature (London) **561**, 507 (2018).
[14] Z. Wu, A. S. Fisher, J. Goodfellow, M. Fuchs, D. Daranciang, M. Hogan, H. Loos, and A. Lindenberg, Rev. Sci. Instrum. **84**, 022701 (2013).
[15] N. Sei, H. Ogawa, T. Sakai, K. Hayakawa, T. Tanaka, Y. Hayakawa, and K. Nogami, Jpn. J. Appl. Phys. **56**, 032401 (2017).
[16] T. Pak, M. Rezaei-Pandari, S. Kim, G. Lee, D. Wi, C. Hojbota, M. Mirzaie, H. Kim, J. Sung, S. Lee *et al.*, Light Sci. Appl. **12**, 37 (2023).
[17] G. Liao, Y. Li, H. Liu, G. Scott, D. Neely, Y. Zhang, B. Zhu, Z. Zhang, C. Armstrong, E. Zemaityte *et al.*, Proc. Natl. Acad. Sci. U.S.A. **116**, 10 (2019).
[18] J. A. Fülöp, L. Pálfalvi, S. Klingebiel, G. Almási, F. Krausz, S. Karsch, and J. Hebling, Opt. Lett. **37**, 557 (2012).
[19] B. Zhang, Z. Ma, J. Ma, X. Wu, C. Ouyang, D. Kong, T. Hong, X. Wang, P. Yang, L. Chen *et al.*, Laser Photonics Rev. **15**, 2000295 (2021).
[20] X. Wu, D. Kong, S. Hao, Y. Zeng, X. Yu, B. Zhang, M. Dai, S. Liu, J. Wang, Z. Ren *et al.*, Adv. Mater. **8**, 2208947 (2023).
[21] C. Vicario, A. V. Ovchinnikov, S. I. Ashitkov, M. B. Agranat, V. E. Fortov, and C. P. Hauri, Opt. Lett. **39**, 6632 (2014).
[22] A. Pukhov, A. Golovanov, and I. Kostyukov, Phys. Rev. Lett. **127**, 175001 (2021).
[23] Z. M. Sheng, H. C. Wu, K. Li, and J. Zhang, Phys. Rev. E **69**, 025401(R) (2004).
[24] Z. M. Sheng, K. Mima, J. Zhang, and H. Sanuki, Phys. Rev. Lett. **94**, 095003 (2005).
[25] Z. M. Sheng, K. Mima, and J. Zhang, Phys. Plasmas, **12**, 123103 (2005).
[26] H. Hamster, A. Sullivan, S. Gordon, W. White, and R. W. Falcone, Phys. Rev. Lett. **71**, 2725 (1993).
[27] H. Hamster, A. Sullivan, S. Gordon, and R. W. Falcone, Phys. Rev. E **49**, 671 (1994).
[28] Z. Lei, Z. Jin, A. Zhidkov, N. Pathak, Y. Mizuta, K. Huang, N. Nakanii, I. Daito, M. Kando, and T. Hosokai, Prog. Theor. Exp. Phys. **2023**, 033J01 (2023).
[29] K. Wang and D. Mittleman, Nature (London) **432**, 376 (2004).
[30] P. Sprangle, E. Esarey, and A. Ting, Phys. Rev. Lett. **64**, 2011 (1990).
[31] E. Esarey, C. B. Schroeder, and W. P. Leemans, Rev. Mod. Phys. **81**, 1229 (2009).
[32] Z. D. Hu, Z. M. Sheng, W. M. Wang, L. M. Chen, Y. T. Li, and J. Zhang, Phys. Plasmas **20**, 080702 (2013).
[33] M. Chen, Z. M. Sheng, Y. Y. Ma, and J. Zhang, J. Appl. Phys. **99**, 056109 (2006).
[34] A. Pak, K. A. Marsh, S. F. Martins, W. Lu, W. B. Mori, and C. Joshi, Phys. Rev. Lett. **104**, 025003 (2010).
[35] M. Mirzaie, S. Li, M. Zeng, N. Hafz, M. Chen, G. Y. Li, Q. J. Zhu, H. Liao, T. Sokollik, F. Liu *et al.*, Sci. Rep. **5**, 14659 (2015).
[36] R. A. Fonseca, L. O. Silva, F. S. Tsung, V. K. Decyk, W. Lu, C. Ren, W. B. Mori, S. Deng, S. Lee, and T. Katsouleas, Lect. Notes Comput. Sci. **2331**, 342 (2002); R. G. Hemker, Particle-in-cell modeling of plasma-based accelerators in two and three dimensions, Ph.D. dissertation UCLA, 1999, arXiv:1503.00276.
[37] C. J. Zhang, J. F. Hua, Y. Wan, C. H. Pai, B. Guo, J. Zhang, Y. Ma, F. Li, Y. P. Wu, H. H. Chu, Y. Q. Gu, X. L. Xu, W. B. Mori, C. Joshi, J. Wang, and W. Lu, Phys. Rev. Lett. **119**, 064801 (2017).
[38] N. H. Matlis, G. R. Plateau, J. van Tilborg, C. G. R. Geddes, Cs. Tóth, C. B. Schroeder, E. Esarey, and W. P. Leemans, *AIP Conf. Proc.* 1086, 713 (2009).
[39] B. Zhao, M. Hu, X. Ao, N. Chen, and G. Pei, Appl. Energy **236**, 489 (2019).